

Probing electroweak phase transition with multi-TeV muon colliders and gravitational waves

Wei Liu,^a Ke-Pan Xie^b

^a*Department of Applied Physics, Nanjing University of Science and Technology, Nanjing 210094, People's Republic of China*

^b*Center for Theoretical Physics, Department of Physics and Astronomy, Seoul National University, Seoul 08826, Korea*

E-mail: wei.liu@njust.edu.cn, kpxie@snu.ac.kr

ABSTRACT: We study the complementarity of the proposed multi-TeV muon colliders and the near-future gravitational wave (GW) detectors to the first order electroweak phase transition (FOEWPT), taking the real scalar extended Standard Model as the representative model. A detailed collider simulation shows the FOEWPT parameter space can be greatly probed via the vector boson fusion production of the singlet, and its subsequent decay to the di-Higgs or di-boson channels. Especially, almost all the parameter space yielding detectable GW signals can be probed by the muon colliders. Therefore, if we could detect stochastic GWs in the future, a muon collider could provide a hopeful crosscheck to identify their origin. On the other hand, there is considerable parameter space that escapes GW detections but is within the reach of the muon colliders. The precision measurements of Higgs couplings could also probe the FOEWPT parameter space efficiently.

Contents

1	Introduction	1
2	FOEWPT in the xSM	2
2.1	The model	2
2.2	FOEWPT and GWs	3
3	Phenomenology at high energy muon colliders	6
3.1	Production and decays of the heavy scalar	6
3.2	Direct search: the $h_2 \rightarrow h_1 h_1 \rightarrow b\bar{b}b\bar{b}$ channel	8
3.3	Direct search: the $h_2 \rightarrow ZZ \rightarrow \ell^+ \ell^- \ell^+ \ell^-$ channel	10
3.4	Indirect search: the Higgs coupling deviations	12
4	Conclusion	13
A	Deriving the phenomenologically allowed potential	14

1 Introduction

Revealing the nature of the electroweak phase transition (EWPT) is one of the most important tasks in particle physics after the discovery of the Higgs boson at the LHC [1, 2]. In the Standard Model (SM), lattice calculations have shown that the EWPT is a smooth crossover [3–5]. However, the EWPT could be first-order (FO) in many new physics models beyond the SM (BSM), such as the real singlet extended SM (xSM) [6–20], two-Higgs-doublet model [21–34], left-right symmetric model [35, 36]¹, Georgi-Machacek model [38] and composite Higgs models [39–46], etc. A FOEWPT can drive the early Universe out of thermal equilibrium, providing the essential environment for the electroweak baryogenesis (EWBG) mechanism [47–49], which explains the observed cosmological matter-antimatter asymmetry.

The FOEWPT can manifest itself at two different kinds of experiments: the gravitational wave (GW) detectors and the high energy particle colliders. In the former case, the stochastic GWs generated during the FOEWPT are expected to be detectable at a few near-future space-based laser interferometers such as LISA [50], BBO [51], TianQin [52, 53], Taiji [54, 55] and DECIGO [56, 57]. While in the latter case, the BSM physics related to FOEWPT might be probed at the colliders [58], such as the CERN LHC and future proton-proton colliders including HE-LHC [59], SppC [60] and FCC-hh [61], or future electron-positron colliders such as CEPC [62], ILC [63] and FCC-ee [64]. Generally speaking, the hadron colliders have high energy reach but suffer from the huge QCD backgrounds, while

¹A research for the Pati-Salam model can be found in Ref. [37].

the electron-positron colliders are very accurate but limited by the relatively low collision energy due to the large synchrotron radiation.

A muon collider might be able to offer both high collision energy and clean environment to probe the FOEWPT. On one hand, thanks to the suppressed synchrotron radiation compared to the electron, the energy of a muon collider can reach $\mathcal{O}(10)$ TeV. What's more, the entire muon collision energy can be used to probe the short-distance reactions (hard processes). In contrast, at a pp collider such as LHC, only a small fraction of the proton collision energy is available for the hard processes. On the other hand, due to the small QCD backgrounds, the muon collider is rather clean, allowing very precise measurements. The physics potential of a high energy muon collider has been discussed since the 1990s [65, 66], while it receives a renewed interest recently [67–84].

In this work, we investigate the possibility of probing FOEWPT at a multi-TeV muon collider and the complementarity with the GW experiments, taking the xSM as the benchmark model. Although the xSM is simple, it has captured the most important features of the FOEWPT induced by tree level barrier via renormalizable operators [85], and can serve as the prototype of many BSM models that trigger the FOEWPT. For the muon collider setup, we follow Ref. [78] to consider collision energies of 3, 6, 10 and 30 TeV, with integrated luminosities of 1, 4, 10 and 90 ab^{-1} , respectively.

This paper is organized as follows. We first introduce the xSM and derive its parameter space for FOEWPT in Section 2, where we also discuss the GW signals and their detectability at the future LISA detector. The phenomenology at high energy muon colliders is studied in Section 3, where both the direct (i.e. resonant production of the real singlet) and indirect (i.e. the Higgs coupling measurements) searches are considered. The complementarity between collider and GW experiments is also discussed. Finally, we conclude in Section 4.

2 FOEWPT in the xSM

2.1 The model

Up to renormalizable level, the scalar potential of xSM can be generally written as

$$V = -\mu^2|H|^2 + \lambda|H|^4 + \frac{a_1}{2}|H|^2S + \frac{a_2}{2}|H|^2S^2 + b_1S + \frac{b_2}{2}S^2 + \frac{b_3}{3}S^3 + \frac{b_4}{4}S^4, \quad (2.1)$$

which has eight input parameters. However, one degree of freedom is unphysical due to the shift invariance of the potential under $S \rightarrow S + \sigma$; in addition, the measured Higgs mass $M_h = 125.09$ GeV and vacuum expectation value (VEV) $v = 246$ GeV put another two constraints, leaving us only five free physical input parameters.

To remove the shift invariance, we fix $b_1 = 0$ in Eq. (2.1). In unitary gauge, Eq. (2.1) can be expanded around the VEV, i.e.

$$H = \frac{1}{\sqrt{2}} \begin{pmatrix} 0 \\ v + h \end{pmatrix}, \quad S = v_s + s, \quad (2.2)$$

and then the mass term of the two neutral scalars reads

$$V \supset \frac{1}{2} \begin{pmatrix} h & s \end{pmatrix} \mathcal{M}_s^2 \begin{pmatrix} h \\ s \end{pmatrix}; \quad \mathcal{M}_s^2 = \begin{pmatrix} \frac{\partial^2 V}{\partial h^2} & \frac{\partial^2 V}{\partial h \partial s} \\ \frac{\partial^2 V}{\partial h \partial s} & \frac{\partial^2 V}{\partial s^2} \end{pmatrix}. \quad (2.3)$$

Diagonalizing \mathcal{M}_s^2 yields the mass eigenstates h_1, h_2 and the mixing angle θ between them, namely

$$\begin{pmatrix} h \\ s \end{pmatrix} = U \begin{pmatrix} h_1 \\ h_2 \end{pmatrix}, \quad U = \begin{pmatrix} \cos \theta & -\sin \theta \\ \sin \theta & \cos \theta \end{pmatrix}, \quad (2.4)$$

such that the mass matrix becomes $U^\dagger \mathcal{M}_s^2 U = \text{diag} \{M_{h_1}^2, M_{h_2}^2\}$. Here we assume the lighter state h_1 is the SM Higgs-like boson.

The requirement that (v, v_s) is an extremum of Eq. (2.1) yields two relations [12]

$$\mu^2 = \lambda v^2 + \frac{v_s}{2}(a_1 + a_2 v_s), \quad b_2 = -\frac{1}{4v_s} [v^2(a_1 + 2a_2 v_s) + 4v_s^2(b_3 + b_4 v_s)], \quad (2.5)$$

where the coefficients λ, a_1 and a_2 can be further expressed in terms of M_{h_1}, M_{h_2} and θ ,

$$\begin{aligned} \lambda &= \frac{M_{h_1}^2 c_\theta^2 + M_{h_2}^2 s_\theta^2}{2v^2}, \\ a_1 &= \frac{4v_s}{v^2} \left[v_s^2 \left(2b_4 + \frac{b_3}{v_s} \right) - M_{h_1}^2 s_\theta^2 - M_{h_2}^2 c_\theta^2 \right], \\ a_2 &= \frac{1}{2v_s} \left[\frac{s_{2\theta}}{v} (M_{h_1}^2 - M_{h_2}^2) - a_1 \right], \end{aligned} \quad (2.6)$$

with c_θ and s_θ being short for $\cos \theta$ and $\sin \theta$, respectively. Fixing $M_{h_1} = M_h = 125.09$ GeV and $v = 246$ GeV, we can use the following five parameters

$$\{M_{h_2}, \theta, v_s, b_3, b_4\}, \quad (2.7)$$

as input, and derive other parameters such as μ^2, λ via Eq. (2.5) and Eq. (2.6).

We use the strategy described in Appendix A to obtain the parameter space that satisfies the SM constraints. The dataset is stored in form of a list of the five input parameters in Eq. (2.7), and then used for the calculation of FOEWPT and GWs in the following subsection.

2.2 FOEWPT and GWs

The scalar potential V in Eq. (2.1) receives thermal corrections at finite temperature, becoming

$$\begin{aligned} V_T &= -(\mu^2 - c_H T^2) |H|^2 + \lambda |H|^4 + \frac{a_1}{2} |H|^2 S + \frac{a_2}{2} |H|^2 S^2 \\ &\quad + (b_1 + m_1 T^2) S + \frac{b_2 + c_S T^2}{2} S^2 + \frac{b_3}{3} S^3 + \frac{b_4}{4} S^4, \end{aligned} \quad (2.8)$$

where we only keep the gauge invariant T^2 -order terms [86, 87], and

$$c_H = \frac{3g^2 + g'^2}{16} + \frac{y_t^2}{4} + \frac{\lambda}{2} + \frac{a_2}{24}, \quad c_S = \frac{a_2}{6} + \frac{b_4}{4}, \quad m_1 = \frac{a_1 + b_3}{12}. \quad (2.9)$$

In our convention, $b_1 = 0$, the tadpole term for s only arises at finite temperature. This term is found to be suppressed in most of the parameter space [7, 11], however for completeness we also include it in numerical study. As we will see very soon, the tadpole has a non-negligible impact on the FOEWPT pattern.

Thermal corrections change the vacuum structure of the scalar potential. In suitable parameter space, there exists a critical temperature T_c at which the potential V_T in Eq. (2.8) has two degenerate vacua, one with $h = 0$ (EW-symmetric) and the other with $h \neq 0$ (EW-broken). Initially, the Universe stays in the EW-symmetric vacuum. As the Universe expands and the temperature falls below T_c , the $h \neq 0$ vacuum is energetically preferred and the Universe acquires a probability of decaying to it. The decay rate per unit volume is [88]

$$\Gamma(T) \sim T^4 \left(\frac{S_3(T)}{2\pi T} \right)^{3/2} e^{-S_3(T)/T}, \quad (2.10)$$

where $S_3(T)$ is the Euclidean action of the $O(3)$ -symmetric bounce solution. FOEWPT occurs when the decay rate per Hubble volume reaches $\mathcal{O}(1)$ and hence the EW-broken vacuum bubbles start to nucleate. This defines the nucleation temperature T_n , which satisfies $\Gamma(T_n) = H^4(T_n)$, with $H(T)$ being the Hubble constant at temperature T . For a radiation-dominated Universe and a phase transition at EW scale, T_n can be solved by the approximate relation [89]

$$S_3(T_n)/T_n \approx 140, \quad (2.11)$$

which we take as the criterion for a FOEWPT.

For each data point derived in last subsection, we calculate T_n by solving Eq. (2.11) with the Python package `CosmoTransitions` [90]. Around 10% of the data can trigger a FOEWPT. The left panel of Fig. 1 shows the collection of FOEWPT data points by plotting the initial and final states of the vacuum decay $(0, v_s^i) \rightarrow (v^f, v_s^f)$. For a successful EWBG, the phase transition should be strong [91, 92]

$$v^f/T_n \gtrsim 1, \quad (2.12)$$

such that the EW sphaleron process in the EW-broken vacuum is suppressed. Hereafter we will focus on data points satisfying Eq. (2.12). We found that many data points yield a decay pattern of $(0, 0) \rightarrow (v^f, v_s^f)$, but there are also considerable fraction of data that have $v_s^i \neq 0$. Quantitatively, if we use $|v_s^i/v_s^f| \lesssim 0.01$ as the criterion of a $(0, 0) \rightarrow (v^f, v_s^f)$ FOEWPT, then the fraction of data points falling in this pattern is around 8.8%, while in Ref. [12] the corresponding fraction is 99%. We have checked that the difference comes from the treatment of the thermal tadpole term in Eq. (2.8): we keep this term, while Ref. [12] drops it. Therefore, the tadpole term actually has a considerable impact on the FOEWPT pattern.

A FOEWPT generates stochastic GWs mainly through three sources: bubble collisions, sound waves in the plasma and the magneto-hydrodynamics turbulence [93]. After cosmological redshift, those GWs today typically peak at $f \sim \text{mHz}$ [94], which is the sensitive region of a few next-generation space-based interferometers mentioned in the

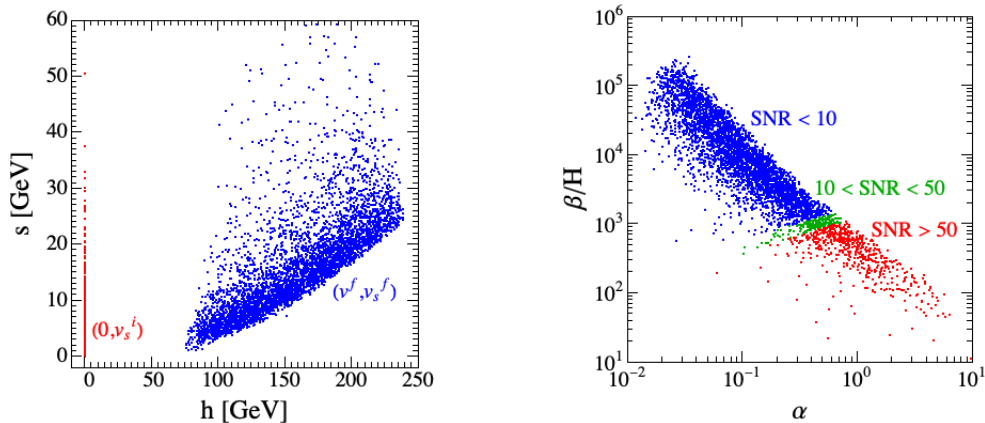


Figure 1. Left: the collection of vacuum decay initial states $(0, v_s^i)$ (red) and final states (v^f, v_s^f) (blue). Right: the SNRs for the SFOEWPT data projected at the α - β/H plane.

introduction. To obtain the GW spectrum today, we derive the following two parameters for each FOEWPT data point

$$\alpha = \frac{1}{g_* \pi^2 T_n^4 / 30} \left(T \frac{\partial \Delta V_T}{\partial T} - \Delta V_T \right) \Big|_{T_n}; \quad \beta/H = T_n \frac{d(S_3/T)}{dT} \Big|_{T_n}, \quad (2.13)$$

where $\Delta V_T = V_T|_{T_n, (v^f, v_s^f)} - V_T|_{T_n, (0, v_s^i)}$ is effective potential difference between the true and false vacua, and $g_* \sim 100$ is the number of relativistic degrees of freedom. In other words, α is the transition latent heat over the radiation energy, while β/H is the Universe expansion time scale over the phase transition duration. Refs. [94–96] point out that the GW spectrum $\Omega_{\text{GW}}(f)$ of a FOEWPT can be expressed as numerical functions of $(\alpha, \beta/H, v_b)$, where v_b is the bubble expansion velocity. Taking $v_b = 0.6$ as a benchmark, we are now able to calculate $\Omega_{\text{GW}}(f)$ for each FOEWPT data point.² The suppression factor coming from the short duration of the sound wave period has been taken into account [102, 103].

The signal-to-noise ratio (SNR) characterizes the detectability of GWs signals at an interferometer. Taking the LISA detector as an example, we calculate the SNR as

$$\text{SNR} = \sqrt{\mathcal{T} \int_{f_{\min}}^{f_{\max}} df \left(\frac{\Omega_{\text{GW}}(f)}{\Omega_{\text{LISA}}(f)} \right)^2}, \quad (2.14)$$

where Ω_{LISA} is the sensitivity curve of the LISA detector [95], and $\mathcal{T} = 9.46 \times 10^7$ s the data-taking duration (around four years) [96]. According to Ref. [95], we use $\text{SNR} > 10$ (50) as the detection threshold for a six-link (four-link) configuration LISA. In the right panel of Fig. 1 we plot the $(\alpha, \beta/H)$ distribution as well as the SNRs of our data points. As shown

²Note that v_b is the bubble velocity with respect to the plasma *at finite distance*, while the velocity relevant for the EWBG calculation is actually v_w , which is defined as the relative velocity to the plasma *just in front of the wall*. The relation between v_b and v_w can be solved using hydrodynamics [97, 98], and it is possible to have a high v_b (good for GW signals) and low v_w (good for EWBG) simultaneously [12, 98–101].

in the figure, the data with large α (which means larger energy released in the transition) and smaller β/H (means longer duration of the transition) have larger SNRs.³

3 Phenomenology at high energy muon colliders

Besides the GWs, the FOEWPT parameter space of the xSM can lead to signals of a resonantly produced heavy scalar (direct search), and corrections to the SM Higgs couplings (indirect search) at the colliders. The corresponding phenomenology has been studied at the LHC and the proposed pp or e^+e^- colliders [11, 12, 99–101, 109–116]. Typically, the direct search is implemented at pp colliders due to their high energy reach, while the indirect approach is preferred by the e^+e^- colliders because of the high accuracy. In this section we will demonstrate that, with the clean background and sufficient collision energy, a multi-TeV muon collider is able to perform both the direct and indirect searches, exhibiting a great potential to test the FOEWPT.

3.1 Production and decays of the heavy scalar

The heavy scalar h_2 can be produced at a lepton collider via the Zh_2 associated production or the vector boson fusion (VBF) process. At a collider with center-of-mass energy as high as a few TeV, the dominant channel is VBF⁴

$$\begin{aligned}\mu^+\mu^- &\rightarrow h_2\nu_\mu\bar{\nu}_\mu \quad (W^+W^- \text{ fusion}), \\ \mu^+\mu^- &\rightarrow h_2\mu^+\mu^- \quad (ZZ \text{ fusion}),\end{aligned}\tag{3.1}$$

and the production rate is

$$\sigma_{h_2} = s_\theta^2 \times \sigma_{h_2}^{\text{SM}},\tag{3.2}$$

where the SM-like production rate $\sigma_{h_2}^{\text{SM}}$ is the SM Higgs VBF production cross section evaluated by replacing the Higgs mass with M_{h_2} . This is because the coupling of h_2 to the SM gauge bosons comes from mixing, see Eq. (2.4). In the left panel of Fig. 2, we have explicitly shown $\sigma_{h_2}^{\text{SM}}$ at the muon collider with different benchmark collision energies \sqrt{s} .⁵ From the figure, it is clear that we can easily obtain hundreds of fb of cross section for h_2 with $\mathcal{O}(\text{TeV})$ mass. For a given \sqrt{s} , the W^+W^- fusion contributes $\sim 90\%$ of the total cross section.

³There are some data points with $\alpha \gtrsim 1$, implying a strong supercooling. In this case, it is suggested that it is the percolation temperature T_p rather than nucleation temperature T_n that should be used to calculate α and β/H [102, 104–107]. Since most of our data lie in the $\alpha \lesssim 1$ region, we adopt the approximation $T_n \approx T_p$, and leave a more detailed treatment for the future work. Also note that we are using the traditional approach to derive FOEWPT profiles and calculate the GWs. It is shown that the alternative dimensional reduction approach can reduce the theoretical uncertainties significantly [108].

⁴The γh_2 associated production (so-called ‘‘radiative return’’) can be comparable to the Zh_2 production at a low energy muon collider [68].

⁵The cross sections are calculated by the MadGraph5aMC@NLO-v2.8.2 event generator [117] with the model file written using FeynRules [118]. The collider simulations in the next two subsections are also implemented with those two packages.

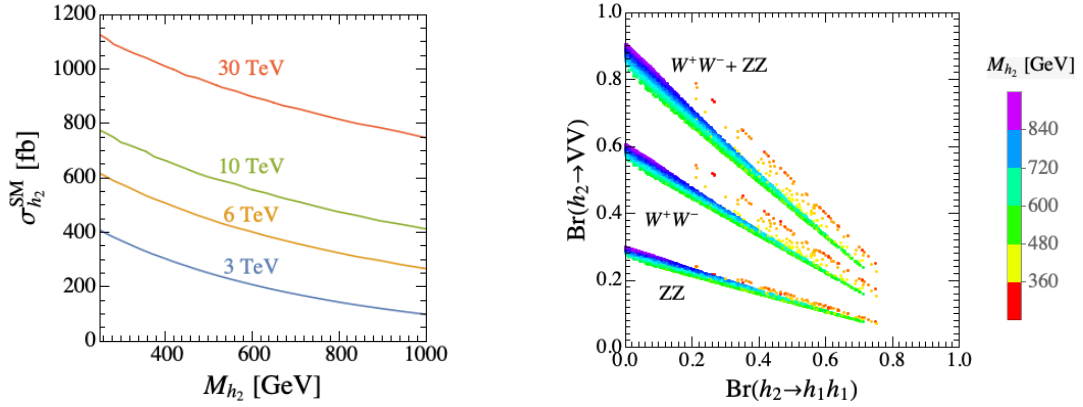


Figure 2. Left: The SM-like production cross section of h_2 at muon colliders with different collision energies. Right: The scattering plots for the $\text{Br}(h_2 \rightarrow VV)$ and $\text{Br}(h_2 \rightarrow h_1h_1)$ corresponding to the FOEWPT data points, and the value of M_{h_2} is shown in color.

The produced h_2 will subsequently decays to multiple final states, such as di-Higgs (h_1h_1), di-boson (W^+W^- and ZZ) and di-fermion (e.g. $t\bar{t}$). For the di-boson and di-fermion channels,

$$\Gamma_{h_2 \rightarrow XX} = s_\theta^2 \times \Gamma_{h_2 \rightarrow XX}^{\text{SM}}, \quad (3.3)$$

where X denotes the SM vector boson or fermion, and $\Gamma_{h_2 \rightarrow XX}^{\text{SM}}$ is the decay width of the SM Higgs calculated at Higgs mass equal to M_{h_2} . For the di-Higgs channel,

$$\Gamma_{h_2 \rightarrow h_1h_1} = \frac{\lambda_{h_2h_1h_1}^2}{32\pi M_{h_2}} \sqrt{1 - \frac{4M_h^2}{M_{h_2}^2}}, \quad (3.4)$$

where the $h_2h_1h_1$ coupling is defined by

$$\mathcal{L}_{\text{xSM}} \supset \frac{1}{2!} \lambda_{h_2h_1h_1} h_2 h_1^2, \quad (3.5)$$

and at tree level [112]

$$\lambda_{h_2h_1h_1} = \left(\frac{1}{2} a_1 + a_2 v_s \right) c_\theta^3 + (2a_2 v - 6\lambda v) s_\theta c_\theta^2 + (6b_4 v_s + 2b_3 - 2a_2 v_s - a_1) s_\theta^2 c_\theta - a_2 v s_\theta^3. \quad (3.6)$$

The branching ratios are

$$\text{Br}(h_2 \rightarrow XX) = \frac{s_\theta^2 \times \Gamma_{h_2 \rightarrow XX}^{\text{SM}}}{s_\theta^2 \times \sum_{X'} \Gamma_{h_2 \rightarrow X'X'}^{\text{SM}} + \Gamma_{h_2 \rightarrow h_1h_1}}, \quad (3.7)$$

$$\text{Br}(h_2 \rightarrow h_1h_1) = \frac{\Gamma_{h_2 \rightarrow h_1h_1}}{s_\theta^2 \times \sum_{X'} \Gamma_{h_2 \rightarrow X'X'}^{\text{SM}} + \Gamma_{h_2 \rightarrow h_1h_1}}. \quad (3.8)$$

The branching ratios of the FOEWPT data points are projected to the $\text{Br}(h_2 \rightarrow h_1h_1)$ - $\text{Br}(h_2 \rightarrow VV)$ plane in the right panel of Fig. 2, where $V = W^\pm, Z$. We see that the

Cross sections [ab]	σ_S^{300}	σ_S^{600}	σ_S^{900}	σ_B^{ZZ}	$\sigma_B^{h_1 h_1}$
No Cut	360	198	155	1080	567
Cut I	123	81.8	84.0	273	96.0
Cut II	104	68.1	69.7	5.42	80.0
Cut III, 300	102			2.43	4.83
Cut III, 600		50.1		$\mathcal{O}(10^{-2})$	5.96
Cut III, 900			35.7	$\mathcal{O}(10^{-2})$	2.96

Table 1. Cut flows at a 10 TeV muon collider for the signals with $M_{h_2} = 300, 600, 900$ GeV and the backgrounds. For the signals, we have assumed $s_\theta = 0.1$ and $\text{Br}(h_2 \rightarrow h_1 h_1) = 25\%$.

di-Higgs branching ratio can reach $\sim 80\%$, while the VV branching ratio dominates for large M_{h_2} . In general, all data points satisfy

$$\text{Br}(h_2 \rightarrow h_1 h_1) + \text{Br}(h_2 \rightarrow VV) + \text{Br}(h_2 \rightarrow t\bar{t}) \approx 100\%, \quad (3.9)$$

and $\text{Br}(h_2 \rightarrow t\bar{t}) \lesssim 20\%$. In the following two subsections, we choose the $h_2 \rightarrow h_1 h_1 \rightarrow b\bar{b}b\bar{b}$ and $h_2 \rightarrow ZZ \rightarrow \ell^+ \ell^- \ell^+ \ell^-$ as two complementary channels for collider simulations.

3.2 Direct search: the $h_2 \rightarrow h_1 h_1 \rightarrow b\bar{b}b\bar{b}$ channel

Directly characterizing the portal coupling between the singlet and the Higgs boson, the $h_2 h_1 h_1$ coupling is of our primary interests. The signal of such a coupling is a resonant di-Higgs production at the muon collider, $\text{VBF} \rightarrow h_2 \rightarrow h_1 h_1$. As the SM Higgs dominantly decays into $b\bar{b}$ pairs, the major final state of the signal consists of four b -jets which can be reconstructed into two h_1 's and then one h_2 . For the ZZ fusion production channel, the final state contains two additional forward muons. Here we focus on the so-called inclusive channel by including both the W^+W^- fusion and ZZ fusion events without detecting the additional muons. In this case, the main backgrounds are the SM VBF $h_1 h_1$ and ZZ production, with $h_1 \rightarrow b\bar{b}$ and $Z \rightarrow b\bar{b}$.⁶

The signal and background events are generated at parton-level. We smear the jet four-momentum according to a jet energy resolution of $\Delta E/E = 10\%$, and assume a conservative b -tagging efficiency rate of 70%. The events are required to have exactly four b -jets satisfying the following basic acceptance cuts,

$$p_T^j > 30 \text{ GeV}, \quad |\eta_j| < 2.43, \quad M_{\text{recoil}} > 200 \text{ GeV}, \quad (\text{Cut I}) \quad (3.10)$$

where the pseudo-rapidity cut is based on a detector angular coverage of $10^\circ < \theta < 170^\circ$, and the recoil mass is defined as

$$M_{\text{recoil}} = \sqrt{(p_{\mu^+} + p_{\mu^-} - p_{j_1} - p_{j_2} - p_{j_3} - p_{j_4})^2}. \quad (3.11)$$

Next, we pair the four b -jets by minimizing

$$\chi_j^2 = (M_{j_1 j_2} - M_h)^2 + (M_{j_3 j_4} - M_h)^2, \quad (3.12)$$

⁶There are also QCD backgrounds such as $4b2\nu_\mu$, but they turn out to be negligible after the Higgs candidates selection [78, 115], thus will not be considered here.

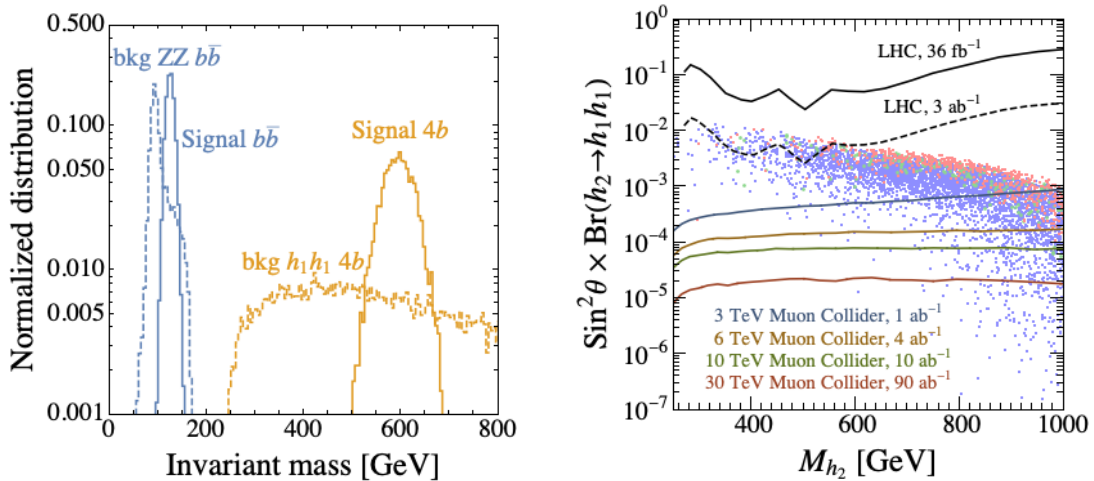


Figure 3. Left: after the basic acceptance cuts, the invariant mass distributions of the jet pairs and four-jet system for the signal and main backgrounds at the 10 TeV muon collider. Here we select $M_{h_2} = 600$ GeV as the signal benchmark. Right: the expected probe limits on $s_\theta^2 \times \text{Br}(h_2 \rightarrow h_1 h_1)$ for different muon collider setups. The scatter points are the FOEWPT data, in which red, green and blue colors represent $\text{SNR} \in [50, +\infty)$, $[10, 50)$ and $[0, 10)$, respectively. The limit from ATLAS at the 13 TeV LHC with $\mathcal{L} = 36.1 \text{ fb}^{-1}$ [119] and its extrapolation to the HL-LHC [12] are also shown for comparison.

The pairs (j_1, j_2) and (j_3, j_4) are then identified as the Higgs candidates, in which the harder pair is defined as (j_1, j_2) . As shown in blue in the left panel of Fig. 3, $M_{j_1 j_2}$ and $M_{j_3 j_4}$ peak around M_h for the signal, while peak around $M_Z = 91.188$ GeV for the ZZ background. Therefore, an invariant mass cut

$$|M_{j_1 j_2} - M_h| < 15 \text{ GeV}, \quad |M_{j_3 j_4} - M_h| < 15 \text{ GeV}, \quad (\text{Cut II}) \quad (3.13)$$

can significantly remove the ZZ background. While most SM $h_1 h_1$ events survive this cut, this background can be removed greatly by the cut on the four-jet system,

$$|M_{4j} - M_{h_2}| < 30 \text{ GeV}, \quad (\text{Cut III}) \quad (3.14)$$

as illustrated in orange in the left panel of Fig. 3. The cut flows for three chosen signal benchmarks at a 10 TeV muon collider are shown in Table 1, indicating Cut III is fairly powerful to improve the signal over background factor.

Given the collision energy \sqrt{s} and the integrated luminosity \mathcal{L} , the signal and background event numbers are

$$\begin{aligned} S &= \sigma_S \times \epsilon_S \times \mathcal{L} = \sigma_{h_2}^{\text{SM}} \times s_\theta^2 \times \text{Br}(h_2 \rightarrow h_1 h_1) \times \epsilon_S \times \mathcal{L}, \\ B &= \sigma_B \times \epsilon_B \times \mathcal{L}, \end{aligned} \quad (3.15)$$

where $\sigma_{S,B}$ are the signal and background production rates, and $\epsilon_{S,B}$ are the corresponding cut efficiencies, respectively. Note that σ_B is already fixed, and $\sigma_{h_2}^{\text{SM}}$ as well as $\epsilon_{S,B}$ depends only on M_{h_2} . This implies that we can generate events for several M_{h_2} benchmarks and

derive the collider probe limits for $s_\theta^2 \times \text{Br}(h_2 \rightarrow h_1 h_1)$, and make the interpolation to derive the $s_\theta^2 \times \text{Br}(h_2 \rightarrow h_1 h_1)$ reach as a function of M_{h_2} . As for the probe limits, we use the Poisson likelihood function

$$L(S) = e^{-(S+B)} \frac{(S+B)^n}{n!} \quad (3.16)$$

with the number of observed events (n) taken to be equal to the background events ($n = B$). To get the 95% confidence level exclusion limits, we use the test statistic Q_k

$$Q_S \equiv -2 \ln \left[\frac{L(S)}{L(0)} \right] = 3.84. \quad (3.17)$$

When $B \gg S$, the above procedure reduces to the well-known $S/\sqrt{B} = 1.96$ criterion. The sensitivity of the muon collider to FOEWPT can be obtained by projecting the FOEWPT parameter space to such 2-dimension plane. This is done in the right panel of Fig. 3, in which the reach of different collider setups are plotted as different colored solid lines, and the FOEWPT data points lying above a specific line can be probed by the corresponding muon collider. Note that our projections are derived with a rather conservative b -tagging efficiency of 70%. A more optimistic efficiency such as 90% can improve the results by a factor of 2, while an analysis without b -tagging will weaken the limits by a factor of 2 or 3, as in this case the non- b jets (such as $W^\pm/Z \rightarrow jj$) also contribute to the backgrounds. However, either case has little visual effects in the log coordinate.

The right panel of Fig. 3 demonstrates that the FOEWPT parameter space can be greatly probed by the muon colliders, and higher energy colliders (with also higher integrated luminosities) give better reach. The current and projected LHC reach is shown in black lines for comparison. Because of the high accuracy in the multi-jet final state, even a 3 TeV muon collider (1 ab^{-1}) has a sensitivity more than one order of magnitude better than the HL-LHC (13 TeV, 3 ab^{-1}), and a 30 TeV muon collider (90 ab^{-1}) is able to probe $s_\theta^2 \times \text{Br}(h_2 \rightarrow h_1 h_1)$ up to 10^{-5} , covering almost all of the FOEWPT parameter space. To manifest the complementarity with the GW experiments, we use different colors to mark the FOEWPT points with different SNRs: red, green and blue for $\text{SNR} \in [50, +\infty)$, $[10, 50)$ and $[0, 10)$, respectively. Treating $\text{SNR} = 10$ as the detectable threshold, we see that those points which can be detected by LISA mostly lie in the reach of the muon colliders, especially for the $\sqrt{s} \geq 6 \text{ TeV}$ setups. This is a great opportunity to identify the origin of the stochastic GWs, if they were detected in the future. On the other hand, the muon colliders also have significant sensitivity to the blue data points which are not detectable at the LISA.

For muon colliders with $\sqrt{s} \leq 10 \text{ TeV}$, there are still appreciable number of points which can not be reached, due to the tiny $\text{Br}(h_2 \rightarrow h_1 h_1)$ in those points. Hence, in the next subsection, we will change our strategy by looking for a complementary decay channel, $h_2 \rightarrow ZZ$, to finally cover those points.

3.3 Direct search: the $h_2 \rightarrow ZZ \rightarrow \ell^+ \ell^- \ell^+ \ell^-$ channel

The FOEWPT data points with tiny $\text{Br}(h_2 \rightarrow h_1 h_1)$ might be potentially probed via the $h_2 \rightarrow W^+ W^-$ or $h_2 \rightarrow ZZ$ channels. To get a better accuracy we focus on the leptonic

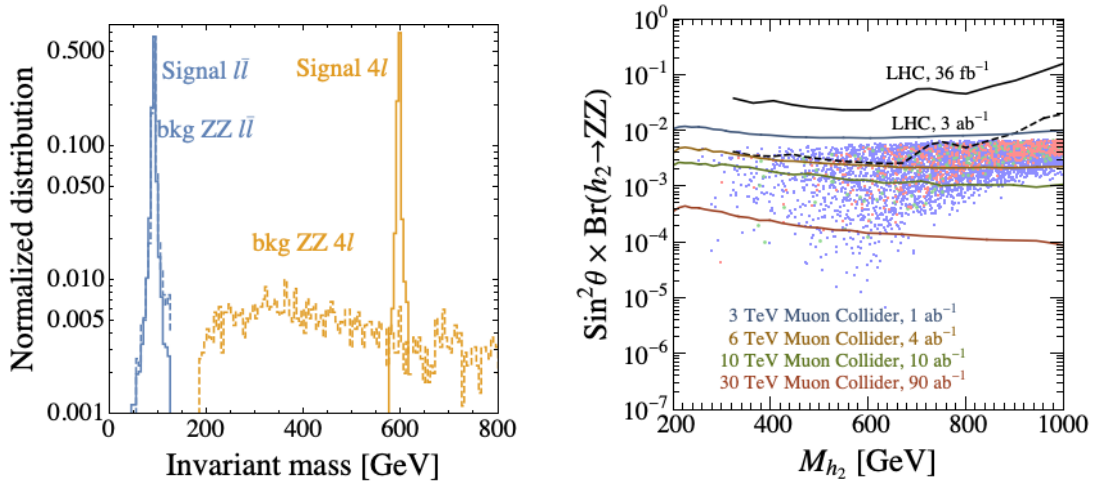


Figure 4. Left: after the basic acceptance cuts, the invariant mass distributions of the lepton pairs and four-lepton system for the signal and main backgrounds at the 10 TeV muon collider. Here we select $M_{h_2} = 600$ GeV as the signal benchmark. Right: the expected probe limits on $s_\theta^2 \times \text{Br}(h_2 \rightarrow ZZ)$ for different muon collider setups. The scatter points are the FOEWPT data, in which red, green and blue colors represent $\text{SNR} \in [50, +\infty)$, $[10, 50)$ and $[0, 10)$, respectively. The limit from ATLAS at the 13 TeV LHC with $\mathcal{L} = 36.1 \text{ fb}^{-1}$ [120] and its extrapolation to the HL-LHC [12] are also shown for comparison..

decay of the gauge bosons. Although the W^+W^- channel has a larger branching ratio, the neutrinos in the final state make this channel more challenging. In this subsection we would like to focus on the ZZ channel with $Z \rightarrow \ell^+\ell^-$, where $\ell = e, \mu$, leading to a four-lepton final state.

Similar to the treatment in the di-Higgs channel in the previous subsection, three cuts are applied to the events. We first require the events to have exactly four charged leptons with total zero charge, and satisfy the acceptance cuts

$$p_T^\ell > 30 \text{ GeV}, \quad |\eta_\ell| < 2.43, \quad M_{\text{recoil}} > 200 \text{ GeV}, \quad (\text{Cut I}) \quad (3.18)$$

where M_{recoil} is defined similarly to Eq. (3.11). We then we pair the opposite-sign leptons by minimizing⁷

$$\chi_\ell^2 = (M_{\ell_1^+\ell_1^-} - M_Z)^2 + (M_{\ell_2^+\ell_2^-} - M_Z)^2, \quad (3.19)$$

and put a second cut

$$|M_{\ell_1^+\ell_1^-} - M_Z| < 10 \text{ GeV}, \quad |M_{\ell_2^+\ell_2^-} - M_Z| < 10 \text{ GeV}, \quad (\text{Cut II}) \quad (3.20)$$

to the events. Note that this cut will select both the signal and background ZZ events. Finally, a cut for the four-lepton system

$$|M_{4\ell} - M_{h_2}| < 20 \text{ GeV}, \quad (\text{Cut III}) \quad (3.21)$$

⁷We don't distinguish the lepton flavors here. We have checked that pairing method which distinguishes the flavors by classifying the same-flavor opposite-charge leptons into a pair [such as $(e^+e^-)(\mu^+\mu^-)$] gives almost the same $M_{\ell^+\ell^-}$ distributions.

can cut away the background significantly, as illustrated in the left panel of Fig. 4.

The collider reach in ZZ channel can be shown as $s_\theta^2 \times \text{Br}(h_2 \rightarrow ZZ)$ limits in the right panel of Fig. 4, in which different colored lines denote different muon collider setups, and the LHC current and future limits are also shown for comparison. Different from the case of $h_1 h_1$ channel, the reach of the HL-LHC is comparable to a 6 TeV muon collider (4 ab^{-1}) for $M_{h_2} \lesssim 650 \text{ GeV}$, thanks to the cleanness of the four-lepton final state. Nevertheless, better sensitivities can still be obtained for muon colliders with $\sqrt{s} \geq 10 \text{ TeV}$, especially for a 30 TeV (90 ab^{-1}) muon collider at which almost all the data points can be probed. We have checked that the FOEWPT data points escaping the $h_1 h_1$ channel search can be generally reached in the ZZ channel; as a result, the combination of $h_1 h_1$ and ZZ channels can cover almost the entire FOEWPT parameter space.⁸ The complementarity with GW experiments are also shown in the figure.

3.4 Indirect search: the Higgs coupling deviations

Besides the direct detection of the heavy scalar h_2 , measuring the couplings of the Higgs-like boson h_1 also give hints of the FOEWPT, as those couplings usually deviate their corresponding SM values in the FOEWPT parameter space. For example, expanding the xSM Lagrangian as

$$\mathcal{L}_{\text{xSM}} \supset \kappa_V \left(M_W^2 W_\mu^+ W^{-\mu} + \frac{1}{2} M_Z^2 Z_\mu Z^\mu \right) \frac{2h_1}{v} - \kappa_3 \frac{M_h^2}{2v} h_1^3, \quad (3.22)$$

at tree level we obtain $\kappa_V = \kappa_3 = 1$ for the SM, while

$$\kappa_V = c_\theta, \quad \kappa_3 = \frac{2v}{M_h^2} \left[\lambda v c_\theta^3 + \frac{1}{4} c_\theta^2 s_\theta (2a_2 v_s + a_1) + \frac{1}{2} a_2 v c_\theta s_\theta^2 + \frac{1}{3} s_\theta^3 (3b_4 v_s + b_3) \right], \quad (3.23)$$

for the xSM. Defining the deviations as

$$\delta\kappa_V = 1 - \kappa_V, \quad \delta\kappa_3 = \kappa_3 - 1, \quad (3.24)$$

we project the FOEWPT data points into the $\delta\kappa_3$ - $\delta\kappa_V$ plane in Fig. 5. One finds that $\delta\kappa_3$ is always positive (and $\lesssim 0.8$). This can be understood by expanding the deviation at small mixing angle [12]

$$\delta\kappa_3 = \theta^2 \left(-\frac{3}{2} + \frac{2M_{h_2}^2 - 2b_3 v_s - 4b_4 v_s^2}{M_h^2} \right) + \mathcal{O}(\theta^3), \quad (3.25)$$

where the $M_{h_2}^2/M_h^2$ term dominates the terms in the bracket, implying an enhanced Higgs triple coupling. Since we set $\theta \leq 0.15$ when scanning over the parameter space (see Appendix A), the $\delta\kappa_V$ distribution has a sharp edge at around $0.15^2/2 \approx 0.01$.

Also shown in Fig. 5 are the projections of the reach for different setups of muon colliders. The corresponding probe limits are adopted from Ref. [78], which uses the

⁸Fig. 4 shows that the 3 TeV muon collider (1 ab^{-1}) fails to probe any FOEWPT data points. This is because we only consider parameter space with a mixing angle $\theta \leq 0.15$. For larger values of θ (such as 0.35 in Ref. [12]), there is reachable parameter space for the 3 TeV muon collider.

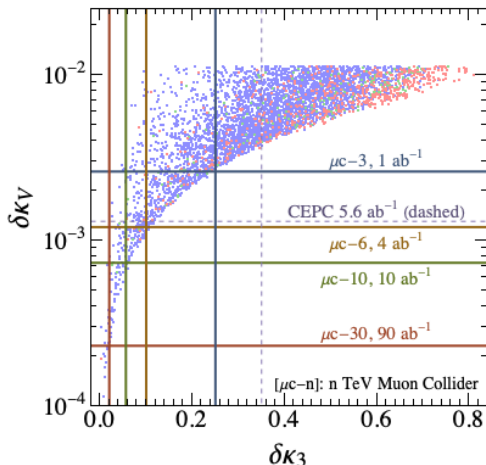


Figure 5. Indirect limits from the measurements of the Higgs couplings. The scatter points are the FOEWPT data, in which red, green and blue colors represent $\text{SNR} \in [50, +\infty)$, $[10, 50)$ and $[0, 10)$, respectively. The colored vertical and horizontal lines are the projections of different setups of muon colliders. The projections of CEPC ($\sqrt{s} = 250$ GeV) are also shown in dashed lines for comparison.

VBF single Higgs production to study the h_1VV coupling and the vector boson scattering di-Higgs production to study the triple Higgs coupling. It is clear that the FOEWPT parameter space can be probed very efficiently using via such indirect approach. A 3 TeV muon collider is already able to cover most of the data points, and a 30 TeV muon collider could test almost the whole parameter space.

4 Conclusion

FOEWPT is an important BSM phenomenon that might exist in the early Universe, and shed light on today’s collider and GW experiments. In this article, we perform a complementarity study of the proposed high energy muon colliders and the near-future space-based GW detectors to the FOEWPT. Choosing the xSM as the benchmark model, we first derive the FOEWPT parameter space, and then test the possibility of detecting it via GW signals or muon collider experiments. In the calculation of FOEWPT, we have included the thermal tadpole term, which is dropped in a few previous references. It is shown that the inclusion of tadpole term reduces the fraction of “ $(0, 0) \rightarrow (v^f, v_s^f)$ pattern” FOEWPT data points from 99% to 8.8%.

A considerable fraction of FOEWPT parameter space yields GW signals with $\text{SNR} \geq 10$ at the LISA detector, thus might be probed. Since the TianQin and Taiji projects in China have projected sensitivities similar to the LISA, we expect the FOEWPT parameter space could be probed and crosschecked by those detectors in the near future.

For the muon colliders, we consider center of mass energies $\sqrt{s} = 3, 6, 10$ and 30 TeV, with corresponding integrated luminosities $\mathcal{L} = 1, 4, 10$ and 90 ab^{-1} , respectively. A detailed parton-level collider simulation is performed for the VBF production of the heavy

real singlet and its subsequent decay to the di-Higgs ($h_2 \rightarrow h_1 h_1 \rightarrow b\bar{b}b\bar{b}$) and di-boson ($h_2 \rightarrow ZZ \rightarrow \ell^+ \ell^- \ell^+ \ell^-$) channels. The results in Figs. 3 and 4 show that muon colliders offer great opportunity to probe the FOEWPT parameter space. In the di-Higgs channel, all muon collider setups have much higher reach compared to the HL-LHC; while in the di-boson channel, the reach of HL-LHC is comparable with a 6 TeV muon collider, however the muon colliders with $\sqrt{s} \geq 10$ TeV still work much better. Combining the di-Higgs and di-boson channels allows us to probe the whole parameter space. In addition, given the high accuracy of the muon colliders, the precision measurements of the Higgs gauge and triple couplings also help to test the FOEWPT.

As for the complementarity with the GW experiments, a remarkable result is that almost all parameter space yielding detectable GWs is within the reach of the muon colliders. This implies if in the future we really detected some signals at the GW detector, a muon collider could provide very useful crosscheck to locate their origin. We also find that there is large parameter space that is not detectable via GWs, but can be probed at the muon colliders.

Acknowledgments

We are grateful to Huai-Ke Guo and Ligong Bian for the very useful discussions and sharing the codes. KPX is supported by the Grant Korea NRF-2019R1C1C1010050.

A Deriving the phenomenologically allowed potential

This appendix demonstrates how to derive the parameter space of a xSM scalar potential that satisfies current phenomenological bounds. In summary, our strategy contains two steps:

1. Construct a potential in Eq. (2.1), and make sure it has a VEV in $(h, s) = (v, 0)$, and a Higgs mass $M_{h_1} = M_h$. In this case, generally $b_1 \neq 0$.
2. Shift the s field such that $b_1 = 0$, and match the new coefficients to the ones described in Eq. (2.7) of Section 2.1. In this case, generally $v_s \neq 0$.

For the first step, an extremum at $(v, 0)$ requires [121]

$$\mu^2 = \lambda v^2, \quad b_1 = -\frac{v^2}{4} a_1; \quad (\text{A.1})$$

and other coefficients can be expressed by the mass eigenvalues and mixing angle

$$a_1 = \frac{s_2 \theta}{v} (M_{h_1}^2 - M_{h_2}^2), \quad b_2 + \frac{a_2}{2} v^2 = M_{h_1}^2 s_\theta^2 + M_{h_2}^2 c_\theta^2, \quad \lambda = \frac{1}{2v^2} (M_{h_1}^2 c_\theta^2 + M_{h_2}^2 s_\theta^2). \quad (\text{A.2})$$

Therefore, we can use

$$\{M_{h_2}, \theta, a_2, b_3, b_4\}, \quad (\text{A.3})$$

as input and derive other coefficients via Eq. (A.1) and Eq. (A.2). We randomly generate the input parameters in the following range:⁹

$$\begin{aligned} M_{h_2} &\in [250, 1000] \text{ GeV}, \quad \theta \in [0, 0.15], \\ b_4 &\in [0, 4\pi/3], \quad a_2 \in [-2\sqrt{\lambda b_4}, 4\pi], \quad |b_3| \in [0, 4\pi v], \end{aligned} \tag{A.4}$$

where the upper limits of a_2 , $|b_3|$ and b_4 come from the unitarity bound [115, 121], while the lower limit of a_2 is required by a bounded below potential [121]. Note that Eq. (A.1) and Eq. (A.2) only guarantee $(v, 0)$ is a local minimum, and there might be another deeper minimum. For a given set of Eq. (A.3), one needs to check whether $(v, 0)$ is the vacuum (i.e. global minimum) by hand. We found that $\sim 38\%$ of the sampling points yield $(v, 0)$ as the vacuum. Such points are then phenomenologically allowed.

For the second step, we shift $s \rightarrow s + \sigma$ to get the following redefinitions of the coefficients in Eq. (2.1) [8],

$$\begin{aligned} \mu^2 &\rightarrow \mu^2 - \frac{1}{2}a_2\sigma^2 - \frac{1}{2}a_1\sigma, \\ a_1 &\rightarrow a_1 + 2a_2\sigma, \\ b_1 &\rightarrow b_1 + b_4\sigma^3 + b_3\sigma^2 + b_2\sigma, \\ b_2 &\rightarrow b_2 + 3b_4\sigma^2 + 2b_3\sigma, \\ b_3 &\rightarrow b_3 + 3b_4\sigma, \end{aligned} \tag{A.5}$$

and choose σ so that the new $b_1 = 0$. As a result, the shifted s has a VEV $v_s = -\sigma$. If a negative v_s is obtained, a \mathbb{Z}_2 transformation $s \rightarrow -s$, $a_1 \rightarrow -a_1$ and $b_3 \rightarrow -b_3$ is further performed to make sure $v_s \rightarrow -v_s$ is positive. Now the new coefficients combined v_s can be matched to the input parameters in Eq. (2.7) for the calculation of FOEWPT and GWs. To check the consistency of our treatment, we have verified that the parameters after shifting satisfy the constraints in Eq. (2.5) and Eq. (2.6).

References

- [1] ATLAS collaboration, G. Aad et al., *Observation of a new particle in the search for the Standard Model Higgs boson with the ATLAS detector at the LHC*, *Phys. Lett. B* **716** (2012) 1–29, [[1207.7214](#)].
- [2] CMS collaboration, S. Chatrchyan et al., *Observation of a New Boson at a Mass of 125 GeV with the CMS Experiment at the LHC*, *Phys. Lett. B* **716** (2012) 30–61, [[1207.7235](#)].
- [3] K. Kajantie, M. Laine, K. Rummukainen and M. E. Shaposhnikov, *A Nonperturbative analysis of the finite T phase transition in $SU(2) \times U(1)$ electroweak theory*, *Nucl. Phys. B* **493** (1997) 413–438, [[hep-lat/9612006](#)].
- [4] K. Rummukainen, M. Tsypin, K. Kajantie, M. Laine and M. E. Shaposhnikov, *The Universality class of the electroweak theory*, *Nucl. Phys. B* **532** (1998) 283–314, [[hep-lat/9805013](#)].

⁹If h_2 is too heavy, its thermal effect will be suppressed by the Boltzmann factor and the high-temperature expansion doesn't apply. Therefore we require $M_{h_2} \leq 1$ TeV.

- [5] M. Laine and K. Rummukainen, *What's new with the electroweak phase transition?*, *Nucl. Phys. B Proc. Suppl.* **73** (1999) 180–185, [[hep-lat/9809045](#)].
- [6] J. McDonald, *Electroweak baryogenesis and dark matter via a gauge singlet scalar*, *Phys. Lett. B* **323** (1994) 339–346.
- [7] S. Profumo, M. J. Ramsey-Musolf and G. Shaughnessy, *Singlet Higgs phenomenology and the electroweak phase transition*, *JHEP* **08** (2007) 010, [[0705.2425](#)].
- [8] J. R. Espinosa, T. Konstandin and F. Riva, *Strong Electroweak Phase Transitions in the Standard Model with a Singlet*, *Nucl. Phys. B* **854** (2012) 592–630, [[1107.5441](#)].
- [9] J. M. Cline and K. Kainulainen, *Electroweak baryogenesis and dark matter from a singlet Higgs*, *JCAP* **01** (2013) 012, [[1210.4196](#)].
- [10] T. Alanne, K. Tuominen and V. Vaskonen, *Strong phase transition, dark matter and vacuum stability from simple hidden sectors*, *Nucl. Phys. B* **889** (2014) 692–711, [[1407.0688](#)].
- [11] S. Profumo, M. J. Ramsey-Musolf, C. L. Wainwright and P. Winslow, *Singlet-catalyzed electroweak phase transitions and precision Higgs boson studies*, *Phys. Rev. D* **91** (2015) 035018, [[1407.5342](#)].
- [12] A. Alves, T. Ghosh, H.-K. Guo, K. Sinha and D. Vagie, *Collider and Gravitational Wave Complementarity in Exploring the Singlet Extension of the Standard Model*, *JHEP* **04** (2019) 052, [[1812.09333](#)].
- [13] V. Vaskonen, *Electroweak baryogenesis and gravitational waves from a real scalar singlet*, *Phys. Rev. D* **95** (2017) 123515, [[1611.02073](#)].
- [14] F. P. Huang, Z. Qian and M. Zhang, *Exploring dynamical CP violation induced baryogenesis by gravitational waves and colliders*, *Phys. Rev. D* **98** (2018) 015014, [[1804.06813](#)].
- [15] W. Cheng and L. Bian, *From inflation to cosmological electroweak phase transition with a complex scalar singlet*, *Phys. Rev. D* **98** (2018) 023524, [[1801.00662](#)].
- [16] T. Alanne, T. Hügler, M. Platscher and K. Schmitz, *A fresh look at the gravitational-wave signal from cosmological phase transitions*, *JHEP* **03** (2020) 004, [[1909.11356](#)].
- [17] O. Gould, J. Kozaczuk, L. Niemi, M. J. Ramsey-Musolf, T. V. Tenkanen and D. J. Weir, *Nonperturbative analysis of the gravitational waves from a first-order electroweak phase transition*, *Phys. Rev. D* **100** (2019) 115024, [[1903.11604](#)].
- [18] M. Carena, Z. Liu and Y. Wang, *Electroweak phase transition with spontaneous Z_2 -breaking*, *JHEP* **08** (2020) 107, [[1911.10206](#)].
- [19] K. Ghorbani and P. H. Ghorbani, *Strongly First-Order Phase Transition in Real Singlet Scalar Dark Matter Model*, *J. Phys. G* **47** (2020) 015201, [[1804.05798](#)].
- [20] P. H. Ghorbani, *Electroweak Baryogenesis and Dark Matter via a Pseudoscalar vs. Scalar*, *JHEP* **08** (2017) 058, [[1703.06506](#)].
- [21] N. Turok and J. Zadrozny, *Electroweak baryogenesis in the two doublet model*, *Nucl. Phys. B* **358** (1991) 471–493.
- [22] N. Turok and J. Zadrozny, *Phase transitions in the two doublet model*, *Nucl. Phys. B* **369** (1992) 729–742.
- [23] J. M. Cline, K. Kainulainen and M. Trott, *Electroweak Baryogenesis in Two Higgs Doublet Models and B meson anomalies*, *JHEP* **11** (2011) 089, [[1107.3559](#)].

- [24] G. Dorsch, S. Huber and J. No, *A strong electroweak phase transition in the 2HDM after LHC8*, *JHEP* **10** (2013) 029, [[1305.6610](#)].
- [25] W. Chao and M. J. Ramsey-Musolf, *Catalysis of Electroweak Baryogenesis via Fermionic Higgs Portal Dark Matter*, [1503.00028](#).
- [26] P. Basler, M. Krause, M. Muhlleitner, J. Wittbrodt and A. Wlotzka, *Strong First Order Electroweak Phase Transition in the CP-Conserving 2HDM Revisited*, *JHEP* **02** (2017) 121, [[1612.04086](#)].
- [27] A. Haarr, A. Kvellestad and T. C. Petersen, *Disfavouring Electroweak Baryogenesis and a hidden Higgs in a CP-violating Two-Higgs-Doublet Model*, [1611.05757](#).
- [28] G. Dorsch, S. Huber, K. Mimasu and J. No, *The Higgs Vacuum Uplifted: Revisiting the Electroweak Phase Transition with a Second Higgs Doublet*, *JHEP* **12** (2017) 086, [[1705.09186](#)].
- [29] J. O. Andersen, T. Gorda, A. Helset, L. Niemi, T. V. I. Tenkanen, A. Tranberg et al., *Nonperturbative Analysis of the Electroweak Phase Transition in the Two Higgs Doublet Model*, *Phys. Rev. Lett.* **121** (2018) 191802, [[1711.09849](#)].
- [30] J. Bernon, L. Bian and Y. Jiang, *A new insight into the phase transition in the early Universe with two Higgs doublets*, *JHEP* **05** (2018) 151, [[1712.08430](#)].
- [31] L. Wang, J. M. Yang, M. Zhang and Y. Zhang, *Revisiting lepton-specific 2HDM in light of muon $g - 2$ anomaly*, *Phys. Lett. B* **788** (2019) 519–529, [[1809.05857](#)].
- [32] X. Wang, F. P. Huang and X. Zhang, *Gravitational wave and collider signals in complex two-Higgs doublet model with dynamical CP-violation at finite temperature*, *Phys. Rev. D* **101** (2020) 015015, [[1909.02978](#)].
- [33] K. Kainulainen, V. Keus, L. Niemi, K. Rummukainen, T. V. Tenkanen and V. Vaskonen, *On the validity of perturbative studies of the electroweak phase transition in the Two Higgs Doublet model*, *JHEP* **06** (2019) 075, [[1904.01329](#)].
- [34] W. Su, A. G. Williams and M. Zhang, *Strong first order electroweak phase transition in 2HDM confronting future Z & Higgs factories*, [2011.04540](#).
- [35] V. Brdar, L. Graf, A. J. Helmboldt and X.-J. Xu, *Gravitational Waves as a Probe of Left-Right Symmetry Breaking*, *JCAP* **12** (2019) 027, [[1909.02018](#)].
- [36] M. Li, Q.-S. Yan, Y. Zhang and Z. Zhao, *Prospects of gravitational waves in the minimal left-right symmetric model*, [2012.13686](#).
- [37] W.-C. Huang, F. Sannino and Z.-W. Wang, *Gravitational Waves from Pati-Salam Dynamics*, *Phys. Rev. D* **102** (2020) 095025, [[2004.02332](#)].
- [38] R. Zhou, W. Cheng, X. Deng, L. Bian and Y. Wu, *Electroweak phase transition and Higgs phenomenology in the Georgi-Machacek model*, *JHEP* **01** (2019) 216, [[1812.06217](#)].
- [39] J. R. Espinosa, B. Gripaios, T. Konstandin and F. Riva, *Electroweak Baryogenesis in Non-minimal Composite Higgs Models*, *JCAP* **01** (2012) 012, [[1110.2876](#)].
- [40] M. Chala, G. Nardini and I. Sobolev, *Unified explanation for dark matter and electroweak baryogenesis with direct detection and gravitational wave signatures*, *Phys. Rev. D* **94** (2016) 055006, [[1605.08663](#)].
- [41] M. Chala, M. Ramos and M. Spannowsky, *Gravitational wave and collider probes of a triplet Higgs sector with a low cutoff*, *Eur. Phys. J. C* **79** (2019) 156, [[1812.01901](#)].

- [42] S. Bruggisser, B. Von Harling, O. Matsedonskyi and G. Servant, *Baryon Asymmetry from a Composite Higgs Boson*, *Phys. Rev. Lett.* **121** (2018) 131801, [[1803.08546](#)].
- [43] S. Bruggisser, B. Von Harling, O. Matsedonskyi and G. Servant, *Electroweak Phase Transition and Baryogenesis in Composite Higgs Models*, *JHEP* **12** (2018) 099, [[1804.07314](#)].
- [44] L. Bian, Y. Wu and K.-P. Xie, *Electroweak phase transition with composite Higgs models: calculability, gravitational waves and collider searches*, *JHEP* **12** (2019) 028, [[1909.02014](#)].
- [45] S. De Curtis, L. Delle Rose and G. Panico, *Composite Dynamics in the Early Universe*, *JHEP* **12** (2019) 149, [[1909.07894](#)].
- [46] K.-P. Xie, L. Bian and Y. Wu, *Electroweak baryogenesis and gravitational waves in a composite Higgs model with high dimensional fermion representations*, *JHEP* **12** (2020) 047, [[2005.13552](#)].
- [47] D. E. Morrissey and M. J. Ramsey-Musolf, *Electroweak baryogenesis*, *New J. Phys.* **14** (2012) 125003, [[1206.2942](#)].
- [48] J. M. Cline, *Baryogenesis*, in *Les Houches Summer School - Session 86: Particle Physics and Cosmology: The Fabric of Spacetime*, 9, 2006. [hep-ph/0609145](#).
- [49] M. Trodden, *Electroweak baryogenesis*, *Rev. Mod. Phys.* **71** (1999) 1463–1500, [[hep-ph/9803479](#)].
- [50] LISA collaboration, P. Amaro-Seoane et al., *Laser Interferometer Space Antenna*, [1702.00786](#).
- [51] J. Crowder and N. J. Cornish, *Beyond LISA: Exploring future gravitational wave missions*, *Phys. Rev. D* **72** (2005) 083005, [[gr-qc/0506015](#)].
- [52] TIANQIN collaboration, J. Luo et al., *TianQin: a space-borne gravitational wave detector*, *Class. Quant. Grav.* **33** (2016) 035010, [[1512.02076](#)].
- [53] Y.-M. Hu, J. Mei and J. Luo, *Science prospects for space-borne gravitational-wave missions*, *Natl. Sci. Rev.* **4** (2017) 683–684.
- [54] W.-R. Hu and Y.-L. Wu, *The Taiji Program in Space for gravitational wave physics and the nature of gravity*, *Natl. Sci. Rev.* **4** (2017) 685–686.
- [55] W.-H. Ruan, Z.-K. Guo, R.-G. Cai and Y.-Z. Zhang, *Taiji program: Gravitational-wave sources*, *Int. J. Mod. Phys. A* **35** (2020) 2050075, [[1807.09495](#)].
- [56] S. Kawamura et al., *The Japanese space gravitational wave antenna: DECIGO*, *Class. Quant. Grav.* **28** (2011) 094011.
- [57] S. Kawamura et al., *The Japanese space gravitational wave antenna DECIGO*, *Class. Quant. Grav.* **23** (2006) S125–S132.
- [58] M. J. Ramsey-Musolf, *The electroweak phase transition: a collider target*, *JHEP* **09** (2020) 179, [[1912.07189](#)].
- [59] FCC collaboration, A. Abada et al., *HE-LHC: The High-Energy Large Hadron Collider: Future Circular Collider Conceptual Design Report Volume 4*, *Eur. Phys. J. ST* **228** (2019) 1109–1382.
- [60] M. Ahmad et al., *CEPC-SPPC Preliminary Conceptual Design Report. 1. Physics and Detector*, .

- [61] FCC collaboration, A. Abada et al., *FCC-hh: The Hadron Collider: Future Circular Collider Conceptual Design Report Volume 3*, *Eur. Phys. J. ST* **228** (2019) 755–1107.
- [62] CEPC STUDY GROUP collaboration, M. Dong et al., *CEPC Conceptual Design Report: Volume 2 - Physics \& Detector*, [1811.10545](#).
- [63] ILC collaboration, G. Aarons et al., *International Linear Collider Reference Design Report Volume 2: Physics at the ILC*, [0709.1893](#).
- [64] FCC collaboration, A. Abada et al., *FCC-ee: The Lepton Collider: Future Circular Collider Conceptual Design Report Volume 2*, *Eur. Phys. J. ST* **228** (2019) 261–623.
- [65] V. D. Barger, M. Berger, J. Gunion and T. Han, *s channel Higgs boson production at a muon muon collider*, *Phys. Rev. Lett.* **75** (1995) 1462–1465, [[hep-ph/9504330](#)].
- [66] V. D. Barger, M. Berger, J. Gunion and T. Han, *Higgs Boson physics in the s channel at $\mu^+\mu^-$ colliders*, *Phys. Rept.* **286** (1997) 1–51, [[hep-ph/9602415](#)].
- [67] T. Han and Z. Liu, *Potential precision of a direct measurement of the Higgs boson total width at a muon collider*, *Phys. Rev. D* **87** (2013) 033007, [[1210.7803](#)].
- [68] N. Chakrabarty, T. Han, Z. Liu and B. Mukhopadhyaya, *Radiative Return for Heavy Higgs Boson at a Muon Collider*, *Phys. Rev. D* **91** (2015) 015008, [[1408.5912](#)].
- [69] M. Ruhdorfer, E. Salvioni and A. Weiler, *A Global View of the Off-Shell Higgs Portal*, *SciPost Phys.* **8** (2020) 027, [[1910.04170](#)].
- [70] L. Di Luzio, R. Gröber and G. Panico, *Probing new electroweak states via precision measurements at the LHC and future colliders*, *JHEP* **01** (2019) 011, [[1810.10993](#)].
- [71] J. P. Delahaye, M. Diemoz, K. Long, B. Mansoulié, N. Pastrone, L. Rivkin et al., *Muon Colliders*, [1901.06150](#).
- [72] K. Long, D. Lucchesi, M. Palmer, N. Pastrone, D. Schulte and V. Shiltsev, *Muon Colliders: Opening New Horizons for Particle Physics*, [2007.15684](#).
- [73] D. Buttazzo, D. Redigolo, F. Sala and A. Tesi, *Fusing Vectors into Scalars at High Energy Lepton Colliders*, *JHEP* **11** (2018) 144, [[1807.04743](#)].
- [74] A. Costantini, F. De Lillo, F. Maltoni, L. Mantani, O. Mattelaer, R. Ruiz et al., *Vector boson fusion at multi-TeV muon colliders*, *JHEP* **09** (2020) 080, [[2005.10289](#)].
- [75] T. Han, Y. Ma and K. Xie, *High Energy Leptonic Collisions and Electroweak Parton Distribution Functions*, [2007.14300](#).
- [76] R. Capdevilla, D. Curtin, Y. Kahn and G. Krnjaic, *A Guaranteed Discovery at Future Muon Colliders*, [2006.16277](#).
- [77] T. Han, Z. Liu, L.-T. Wang and X. Wang, *WIMPs at High Energy Muon Colliders*, [2009.11287](#).
- [78] T. Han, D. Liu, I. Low and X. Wang, *Electroweak Couplings of the Higgs Boson at a Multi-TeV Muon Collider*, [2008.12204](#).
- [79] N. Bartosik et al., *Detector and Physics Performance at a Muon Collider*, *JINST* **15** (2020) P05001, [[2001.04431](#)].
- [80] M. Chiesa, F. Maltoni, L. Mantani, B. Mele, F. Piccinini and X. Zhao, *Measuring the quartic Higgs self-coupling at a multi-TeV muon collider*, *JHEP* **09** (2020) 098, [[2003.13628](#)].

- [81] W. Yin and M. Yamaguchi, *Muon $g - 2$ at multi-TeV muon collider*, [2012.03928](#).
- [82] D. Buttazzo and P. Paradisi, *Probing the muon $g-2$ anomaly at a Muon Collider*, [2012.02769](#).
- [83] M. Lu, A. M. Levin, C. Li, A. Agapitos, Q. Li, F. Meng et al., *The physics case for an electron-muon collider*, [2010.15144](#).
- [84] G.-y. Huang, F. S. Queiroz and W. Rodejohann, *Gauged $L_\mu - L_\tau$ at a muon collider*, [2101.04956](#).
- [85] D. J. Chung, A. J. Long and L.-T. Wang, *125 GeV Higgs boson and electroweak phase transition model classes*, *Phys. Rev. D* **87** (2013) 023509, [[1209.1819](#)].
- [86] L. Dolan and R. Jackiw, *Symmetry Behavior at Finite Temperature*, *Phys. Rev. D* **9** (1974) 3320–3341.
- [87] E. Braaten and R. D. Pisarski, *Resummation and Gauge Invariance of the Gluon Damping Rate in Hot QCD*, *Phys. Rev. Lett.* **64** (1990) 1338.
- [88] A. D. Linde, *Decay of the False Vacuum at Finite Temperature*, *Nucl. Phys. B* **216** (1983) 421.
- [89] M. Quiros, *Finite temperature field theory and phase transitions*, in *ICTP Summer School in High-Energy Physics and Cosmology*, pp. 187–259, 1, 1999. [hep-ph/9901312](#).
- [90] C. L. Wainwright, *CosmoTransitions: Computing Cosmological Phase Transition Temperatures and Bubble Profiles with Multiple Fields*, *Comput. Phys. Commun.* **183** (2012) 2006–2013, [[1109.4189](#)].
- [91] G. D. Moore, *Measuring the broken phase sphaleron rate nonperturbatively*, *Phys. Rev. D* **59** (1999) 014503, [[hep-ph/9805264](#)].
- [92] R. Zhou, L. Bian and H.-K. Guo, *Connecting the electroweak sphaleron with gravitational waves*, *Phys. Rev. D* **101** (2020) 091903, [[1910.00234](#)].
- [93] A. Mazumdar and G. White, *Review of cosmic phase transitions: their significance and experimental signatures*, *Rept. Prog. Phys.* **82** (2019) 076901, [[1811.01948](#)].
- [94] C. Grojean and G. Servant, *Gravitational Waves from Phase Transitions at the Electroweak Scale and Beyond*, *Phys. Rev. D* **75** (2007) 043507, [[hep-ph/0607107](#)].
- [95] C. Caprini et al., *Science with the space-based interferometer eLISA. II: Gravitational waves from cosmological phase transitions*, *JCAP* **04** (2016) 001, [[1512.06239](#)].
- [96] C. Caprini et al., *Detecting gravitational waves from cosmological phase transitions with LISA: an update*, *JCAP* **03** (2020) 024, [[1910.13125](#)].
- [97] J. R. Espinosa, T. Konstandin, J. M. No and G. Servant, *Energy Budget of Cosmological First-order Phase Transitions*, *JCAP* **06** (2010) 028, [[1004.4187](#)].
- [98] J. M. No, *Large Gravitational Wave Background Signals in Electroweak Baryogenesis Scenarios*, *Phys. Rev. D* **84** (2011) 124025, [[1103.2159](#)].
- [99] A. Alves, T. Ghosh, H.-K. Guo and K. Sinha, *Resonant Di-Higgs Production at Gravitational Wave Benchmarks: A Collider Study using Machine Learning*, *JHEP* **12** (2018) 070, [[1808.08974](#)].
- [100] A. Alves, D. Gonçalves, T. Ghosh, H.-K. Guo and K. Sinha, *Di-Higgs Production in the $4b$ Channel and Gravitational Wave Complementarity*, *JHEP* **03** (2020) 053, [[1909.05268](#)].

- [101] A. Alves, D. Gonçalves, T. Ghosh, H.-K. Guo and K. Sinha, *Di-Higgs Blind Spots in Gravitational Wave Signals*, [2007.15654](#).
- [102] J. Ellis, M. Lewicki and J. M. No, *On the Maximal Strength of a First-Order Electroweak Phase Transition and its Gravitational Wave Signal*, *JCAP* **04** (2019) 003, [[1809.08242](#)].
- [103] H.-K. Guo, K. Sinha, D. Vagie and G. White, *Phase Transitions in an Expanding Universe: Stochastic Gravitational Waves in Standard and Non-Standard Histories*, [2007.08537](#).
- [104] A. Megevand and S. Ramirez, *Bubble nucleation and growth in very strong cosmological phase transitions*, *Nucl. Phys. B* **919** (2017) 74–109, [[1611.05853](#)].
- [105] A. Kobakhidze, C. Lagger, A. Manning and J. Yue, *Gravitational waves from a supercooled electroweak phase transition and their detection with pulsar timing arrays*, *Eur. Phys. J. C* **77** (2017) 570, [[1703.06552](#)].
- [106] J. Ellis, M. Lewicki and J. M. No, *Gravitational waves from first-order cosmological phase transitions: lifetime of the sound wave source*, *JCAP* **07** (2020) 050, [[2003.07360](#)].
- [107] X. Wang, F. P. Huang and X. Zhang, *Phase transition dynamics and gravitational wave spectra of strong first-order phase transition in supercooled universe*, *JCAP* **05** (2020) 045, [[2003.08892](#)].
- [108] D. Croon, O. Gould, P. Schicho, T. V. I. Tenkanen and G. White, *Theoretical uncertainties for cosmological first-order phase transitions*, [2009.10080](#).
- [109] Q.-H. Cao, F. P. Huang, K.-P. Xie and X. Zhang, *Testing the electroweak phase transition in scalar extension models at lepton colliders*, *Chin. Phys. C* **42** (2018) 023103, [[1708.04737](#)].
- [110] L. Bian, H.-K. Guo, Y. Wu and R. Zhou, *Gravitational wave and collider searches for electroweak symmetry breaking patterns*, *Phys. Rev. D* **101** (2020) 035011, [[1906.11664](#)].
- [111] N. Chen, T. Li, Y. Wu and L. Bian, *Complementarity of the future e^+e^- colliders and gravitational waves in the probe of complex singlet extension to the standard model*, *Phys. Rev. D* **101** (2020) 075047, [[1911.05579](#)].
- [112] P. Huang, A. J. Long and L.-T. Wang, *Probing the Electroweak Phase Transition with Higgs Factories and Gravitational Waves*, *Phys. Rev. D* **94** (2016) 075008, [[1608.06619](#)].
- [113] J. Kozaczuk, M. J. Ramsey-Musolf and J. Shelton, *Exotic Higgs boson decays and the electroweak phase transition*, *Phys. Rev. D* **101** (2020) 115035, [[1911.10210](#)].
- [114] A. Papaefstathiou and G. White, *The Electro-Weak Phase Transition at Colliders: Confronting Theoretical Uncertainties and Complementary Channels*, [2010.00597](#).
- [115] J. No and M. Spannowsky, *Signs of heavy Higgs bosons at CLIC: An e^+e^- road to the Electroweak Phase Transition*, *Eur. Phys. J. C* **79** (2019) 467, [[1807.04284](#)].
- [116] K.-P. Xie, *Lepton-mediated electroweak baryogenesis, gravitational waves and the 4π final state at the collider*, [2011.04821](#).
- [117] J. Alwall, R. Frederix, S. Frixione, V. Hirschi, F. Maltoni, O. Mattelaer et al., *The automated computation of tree-level and next-to-leading order differential cross sections, and their matching to parton shower simulations*, *JHEP* **07** (2014) 079, [[1405.0301](#)].
- [118] A. Alloul, N. D. Christensen, C. Degrande, C. Duhr and B. Fuks, *FeynRules 2.0 - A complete toolbox for tree-level phenomenology*, *Comput. Phys. Commun.* **185** (2014) 2250–2300, [[1310.1921](#)].

- [119] ATLAS collaboration, G. Aad et al., *Combination of searches for Higgs boson pairs in pp collisions at $\sqrt{s}=13$ TeV with the ATLAS detector*, *Phys. Lett. B* **800** (2020) 135103, [[1906.02025](#)].
- [120] ATLAS collaboration, M. Aaboud et al., *Combination of searches for heavy resonances decaying into bosonic and leptonic final states using 36 fb^{-1} of proton-proton collision data at $\sqrt{s}=13$ TeV with the ATLAS detector*, *Phys. Rev. D* **98** (2018) 052008, [[1808.02380](#)].
- [121] I. M. Lewis and M. Sullivan, *Benchmarks for Double Higgs Production in the Singlet Extended Standard Model at the LHC*, *Phys. Rev. D* **96** (2017) 035037, [[1701.08774](#)].